

## *Retraction*

# **Retracted: Interpolation Method for Visual Simulation of Engine Exhaust Flame**

### **Journal of Sensors**

Received 13 September 2023; Accepted 13 September 2023; Published 14 September 2023

Copyright © 2023 Journal of Sensors. This is an open access article distributed under the Creative Commons Attribution License, which permits unrestricted use, distribution, and reproduction in any medium, provided the original work is properly cited.

This article has been retracted by Hindawi following an investigation undertaken by the publisher [1]. This investigation has uncovered evidence of one or more of the following indicators of systematic manipulation of the publication process:

- (1) Discrepancies in scope
- (2) Discrepancies in the description of the research reported
- (3) Discrepancies between the availability of data and the research described
- (4) Inappropriate citations
- (5) Incoherent, meaningless and/or irrelevant content included in the article
- (6) Peer-review manipulation

The presence of these indicators undermines our confidence in the integrity of the article's content and we cannot, therefore, vouch for its reliability. Please note that this notice is intended solely to alert readers that the content of this article is unreliable. We have not investigated whether authors were aware of or involved in the systematic manipulation of the publication process.

Wiley and Hindawi regrets that the usual quality checks did not identify these issues before publication and have since put additional measures in place to safeguard research integrity.

We wish to credit our own Research Integrity and Research Publishing teams and anonymous and named external researchers and research integrity experts for contributing to this investigation.

The corresponding author, as the representative of all authors, has been given the opportunity to register their agreement or disagreement to this retraction. We have kept a record of any response received.

### **References**

- [1] B. Cheng, X. Hu, Z. Liu, and X. Gong, "Interpolation Method for Visual Simulation of Engine Exhaust Flame," *Journal of Sensors*, vol. 2021, Article ID 8388241, 12 pages, 2021.

## Research Article

# Interpolation Method for Visual Simulation of Engine Exhaust Flame

Bo Cheng,<sup>1,2</sup> Xiaomei Hu ,<sup>3</sup> Zhiqiang Liu,<sup>4</sup> and Xiuliang Gong<sup>2,4</sup>

<sup>1</sup>School of Computer Science, Northwestern Polytechnical University, Xi'an, 710072 Shaanxi, China

<sup>2</sup>The Sixth Institute, 601 Branch of China Aeronautical Science and Technology Corporation, Hohhot 010076, China

<sup>3</sup>Shanghai Key Laboratory of Intelligent Manufacturing and Robotics, School of Mechatronic Engineering and Automation, Shanghai University, Shanghai 200072, China

<sup>4</sup>School of Cybersecurity, Northwestern Polytechnical University, Xi'an, 710072 Shaanxi, China

Correspondence should be addressed to Xiaomei Hu; [huxiaomei@oa.shu.edu.cn](mailto:huxiaomei@oa.shu.edu.cn)

Received 2 September 2021; Revised 18 November 2021; Accepted 24 November 2021; Published 21 December 2021

Academic Editor: Haibin Lv

Copyright © 2021 Bo Cheng et al. This is an open access article distributed under the Creative Commons Attribution License, which permits unrestricted use, distribution, and reproduction in any medium, provided the original work is properly cited.

Propulsive force and exhaust fluid temperature are important indicators in the performance of an engine. An investigation of the effects of propellant composition, plane flight conditions, and engine operating environment on rocket thrust and the range of smoke plume temperature can provide references in the design of engine mechanics at the optimization of propellant composition, in monitoring of target identification and in the evolving of stealth of stealth technology. In order to understand the characteristics of the engine tail flame, a visual simulation of the engine tail flame was carried out by combining the engine operating conditions with the tail flame conditions. Based on the advantages of the bicubic spline interpolation algorithm and the Kriging interpolation algorithm, this paper proposes a hybrid interpolation algorithm, which performs color mapping and three-dimensional space separation in the engine plume data set and model, and visualizes the engine and engine plume. The simulation realizes real-time monitoring of the functions of various engine components through characteristic colors. The research results show that the hybrid interpolation method can effectively visualize the engine exhaust flame. The simulated plume has a relatively obvious temperature peak at 0.7 m, and the temperature of the plume flow field is significantly higher than that of the frozen plume flow field by about 200~1000 K. This shows that the algorithm in this paper helps to visualize the expression of engine tail flame information.

## 1. Introduction

With the continuous development of several years, the advantages of engine optimization and the methods of engine optimization have gradually gained the attention of people. A high-temperature engine as a power unit has been a typical feature of the engine. The engine's temperature pitch reflects its working condition, in which unstable combustion and vibrating combustion can do damage to the engine that should not be ignored. Up to now, most of the aerospace accidents in various countries are caused by rocket engines, which not only waste a lot of manpower and material resources but also damage the international image and cause bad political influence. Therefore, engine optimization problems, such as the intermittent combustion, buzzing phe-

nomenon, and oscillating combustion of rocket engines, urgently need people's attention, early warning, and optimization. The tail flame temperature is an important parameter that characterizes the combustion of a rocket engine. The flame is essentially a high-temperature gas or plasma material. Under normal circumstances, the most direct cause of the different flame colors is the different burning materials. The instability of the combustion caused by the engine starts to damage the performance of the engine is intuitive, destructive, and difficult to control; the oscillating combustion caused by the unstable combustion of the engine is directly harmful to the engine, and it may even cause serious damage. The engine bursts, and the problem of engine oscillation and combustion is extremely difficult to control. This effect is difficult to analyze in advance at the design stage and

can only be constantly corrected through continuous testing. There are many ways to correct, and the most direct method is to change the chemical properties of the propellant. How to improve is the key to the problem. Therefore, the problem of engine optimization is closely related to the real-time dynamic monitoring of engine tail flames.

In order to understand the engine optimization problem in essence, it is necessary to fully understand the dynamic movement process of the engine tail flame. However, the evolution process of the engine tail flame is very complicated, between stable and unstable, which is difficult to grasp. At present, there are many methods for observing the exhaust flame of an engine, such as measuring the jet flow and radiation state through optical measurement; establishing a chemical reaction model; imaging analysis technology and material science technology to monitor the rocket engine assembly process. In order to meet the research needs of the current society, through comparative analysis, this article believes that the current engine optimization research methods need to be optimized: the detection method is more vivid, more stable, simple, and can reflect certain changes. Therefore, the computer simulation method is one of the important methods to study the dynamic monitoring of the engine tail flame. However, the process of using a computer to visually simulate the engine tail flame involves the interpolation of the engine and the transition problem between color levels in the process of mapping the engine tail flame to the color space system. After the grid is divided, there are unknown data on the grid points that need to be interpolated computer simulation algorithms with the appropriate interpolation algorithms in order to obtain more accurate values and better simulation results and to provide clear data for the optimization process.

Experts at home and abroad have done a lot of research on engine plume and interpolation algorithm. Sreehari et al. proposed an algorithm for electronic tomography reconstruction and sparse image interpolation using nonlocal redundancy in images. We adopted a priori framework called plug and play (P&P) to solve these imaging problems in a regularized inversion setting. It is proved that the algorithm produces higher quality reconstructions on simulated and real electron microscope data, as well as improved convergence characteristics compared with other methods [1]. Kiku et al. propose residual interpolation (RI) as an alternative to color difference interpolation. The proposed RI performs interpolation in the "residual" field, where the residual is the difference between the observed and temporarily estimated pixel values. Our hypothesis for RI is that if image interpolation is performed in a domain with a smaller Laplacian energy, its accuracy will increase [2]. Erb et al. proved that the nodes of the nondegenerate Lissajous curve allow unique interpolation and can be used for orthogonality rules in a binary setting. The explicit formula of Lagrangian polynomials allows simple algorithmic schemes to be used to calculate interpolation polynomials. Compared with the established Padua and Xu point schemes, the numerical results of the proposed scheme show similar approximation errors and similar increases in Lebesgue constant [3]. McGranaghan et al. have developed a new optimal

interpolation technique that can estimate the complete high-latitude ionospheric conductance distribution based on the particle data of the National Defense Meteorological Satellite Program. This technology combines the calculation of ionospheric conductivity based on particle precipitation and its error with the background model and its error covariance to infer the complete distribution of ionospheric conductivity at high latitudes [4]. Janssen proposed an adaptive algorithm to recover missing sample values in discrete-time signals. The algorithm can be locally described through an autoregressive process. For a burst of missing samples, when the burst length tends to infinity, the expected quadratic interpolation error for each sample will converge to the signal variance. This method is actually the first step of an iterative algorithm, where in each iterative steps, the current estimate of the missing sample is used to calculate the new estimate. Muhtarov and Kutiev developed an autocorrelation method for temporal interpolation and short-term prediction of ionospheric properties. The autocorrelation function or its normalized autocorrelation coefficient is determined based on the measured data during 20-30 days, and the autocorrelation model is obtained on this basis. Then, use the model to interpolate the missing values in the monthly ionospheric characteristics table and perform interpolation for a given hour by calculating the weighting coefficients of adjacent measured values. This process selects those measured values that have the highest autocorrelation coefficients around the gap [5]. Huang and Chang studied the dissipation characteristics of the  $(k, l)$ -algebraic stable multistep Runge-Kutta method with constrained grid and linear interpolation program and proved the algebraic stable and irreducible multistep Runge-Kutta method. The method is dissipative for finite-dimensional dynamic systems with time delays, thus, extending and unifying some existing results [6]. These studies have provided us with a lot of reference, but because the methods used in related studies are too simple and the source of the data is unknown, the results of the experiments are unconvincing.

Through this article, we propose a color interpolated pseudoimage coding algorithm for visualization of engine tail flame simulations in 3D visualization, color clustering mapping of engine tail flame and color space system, visual color clustering parameters of engine tail flame based on pseudoimage coding algorithm for clustering study, and realize color interpolation of pseudoimage coding and smooth transition of layer slice level, which makes the color transition of the visualized picture of engine tail flame more natural. The color transition of the visualized pseudocolor image of the engine tail flame is smooth, and the visual expression of the image is more natural.

## 2. Interpolation Method for Visual Simulation of Tail Flame

*2.1. Engine Tail Flame.* With the gradual development of industrial engineering technology, many new and more complex physical phenomena have appeared in production and life. For example, during the flight of missiles and other

aircraft, the airflow and aerodynamic were complexes around and inside the missile body, such as flow fluctuations during water treatment, hydropower, and pipeline transportation [7]. There are many problems in mechanics, some of which have not been well solved in scientific research, and some or due to various reasons, there is no way to conduct ground experimental research [8, 9]. Such problems, more accurate simulations are possible, however, through statistical processes and calculations that can then be learned and finally well established. As of today, the development of high rate computer technology is driving many analytical software to be capital for other public areas of the field such as automotive design, oil industry, biomedical industry, space technology, chemical industry, and other many other engineering sectors.

The flame flow field of the engine rocket belongs to the high Reynolds number and the flow state of the compressed turbulence is complex, including not only the transportation of various components in the gas but also the ignition reaction of the tail flame flow field [10, 11]. The turbulence model is used to simulate the flow of the plume flow field, and the finite rate chemical reaction model is used to simulate the resurgence of the plume flow field.

Propellants in the engine body at high temperature for the formation of high-pressure ingredients complex combustion products, which enter the open atmosphere following the departure of the engine body through the nozzle, forming a section formed by combination of combustion products, components and physical parameters, and the surrounding atmospheric space of material very different, a high temperature and high-pressure mixture in the formation of combustion products from the outside of the nozzle, was called tail jet flame area. The components of the jet flame area are used as the scattering medium, and its optical properties are of great significance to the research objectives of this chapter [12, 13]. As a result of studying the solid engine tail jet flame section, there is an easy way to know that there is a large difference on temperature in different jet flame layer regions, which can have a direct effect on the optical characteristics of the scattering dielectric. The complex refractive index data of particles at some wavelengths is shown in Table 1.

The temperature data of the existing solid engine-tail jet flame flow field was interpolated linearly of the temperature data to obtain the complex refractive error data of each particle in the flow field, and the temperature field effect on the optical parameters of dispersion medium was normalized to a computation model [14]. The rocket plume formation is shown in Figure 1.

Asymptotic color coding-based data system for greenhouse gases flame data set light coding steps involves (1) segmenting the level set of greenhouse data [15]. In which mapping relations between grayscale differences and slice values are divided. (2) Color measurement parameters are computed for the grayscale set using an image of encoding algorithm. (3) The electronic data set that is analyzed using an elaborate interpolation algorithm to improve the show algorithm [16]. The algorithm flow is shown in Figure 2.

**2.2. Bilinear Interpolation Algorithm.** With the bilinear interpolation algorithm, we first perform a linear correlation calculation with the grayscale values of different images that are at the  $y$ -axis position and later perform a linear interpolation calculation over the grayscale values of different types of images at the  $X$ -position, with the input at the  $X$ -position not easily and the  $Y$ -position of the same time [15]. Whether it is the position of position  $X$  or the position of  $Y$ , it has nothing to do with the calculation method of the interpolation algorithm. The interpolation algorithm of  $x$ -axis position and  $y$ -axis position is calculated as follows.

Formula for  $x$ -axis position:

$$f(R_1) = \frac{x_2 - x_1}{x_2 - x_1} f(T_{11}) + \frac{x - x_1}{x_2 - x_1} f((T_{21})), R_1 = (x, y), \quad (1)$$

$$f(R_2) = \frac{x_2 - x_1}{x_2 - x_1} f(T_{12}) + \frac{x - x_1}{x_2 - x_1} f((T_{22})), R_2 = (x, y_2). \quad (2)$$

Formula for  $y$ -axis position:

$$f(P) = \frac{y_2 - y}{y_2 - y_1} f(R_1) + \frac{y - y_1}{y_2 - y_1} f(R_2). \quad (3)$$

If in two-dimensional coordinates, the four obtained values of (0,0), (0,1), (1,0), and (1,1) are used, then, the interpolation formula can be simplified to

$$F(x, y) = f(0, 0)(1 - x)(1 - y) + f(0, 1)(1 - x)y + f(1, 1)xy + f(1, 0)x(1 - y). \quad (4)$$

**2.3. Bicubic Interpolation Algorithm.** In calculating the grayscale values, the bidimensional interpolation algorithm is not considering the conversion rate of the adjacent particle to the image values and the inability to reduce the effect of particles [17]. With high precision, we developed a bicubic interpolation for maintaining fine-grained edge details of image edges and smoother edge. The calculation method is as follows:

$$A = [SW(1 + u) \ SW(u) \ SW(1 - u) \ SW(2 - u)], \quad (5)$$

$$C = [SW(1 + v) \ SW(v) \ SW(1 - v) \ SW(2 - v)], \quad (6)$$

$$B = \begin{cases} f(x - 1, y - 1) & f(x - 1, y) & f(x - 1, y + 1) & f(x - 1, y + 2), \\ f(x, y - 1) & f(x, y) & f(x, y + 1) & f(x, y + 2), \\ f(x + 1, y - 1) & f(x + 1, y) & f(x + 1, y + 1) & f(x + 1, y + 2), \\ f(x + 2, y - 1) & f(x + 1, y) & f(x + 2, y + 1) & f(x + 2, y + 2). \end{cases} \quad (7)$$

Then, the gray value at the sampling point is approximately calculated as  $f(x, y) = A * B * C$ , where

$$S(w) = \begin{cases} 1 - 2|w| + |w| & |w| < 1, \\ 4 - 8|w| + 5|w| & 1 \leq |w| < 2, \\ 0 & |w| \geq 2. \end{cases} \quad (8)$$

TABLE 1: Complex refractive index data at some wavelengths in a high-temperature environment.

Temperature $T$ (K)	Wavelength $\lambda$ ( $\mu\text{m}$ )	Refractive index nm	Absorption coefficient km (i)
2000	0.5	1.54	$5.70 \times 10^{-4}$
	1.0	1.51	$2.64 \times 10^{-4}$
	2.0	1.50	$1.49 \times 10^{-4}$
2300	0.5	1.55	$2.68 \times 10^{-3}$
	1.0	1.52	$1.16 \times 10^{-3}$
	2.0	1.50	$7.29 \times 10^{-4}$
2800	0.5	1.56	$4.54 \times 10^{-3}$
	1.0	1.53	$2.01 \times 10^{-3}$
	2.0	1.51	$1.08 \times 10^{-3}$
3000	0.5	1.58	$1.02 \times 10^{-2}$
	1.0	1.55	$3.58 \times 10^{-3}$
	2.0	1.53	$2.40 \times 10^{-3}$

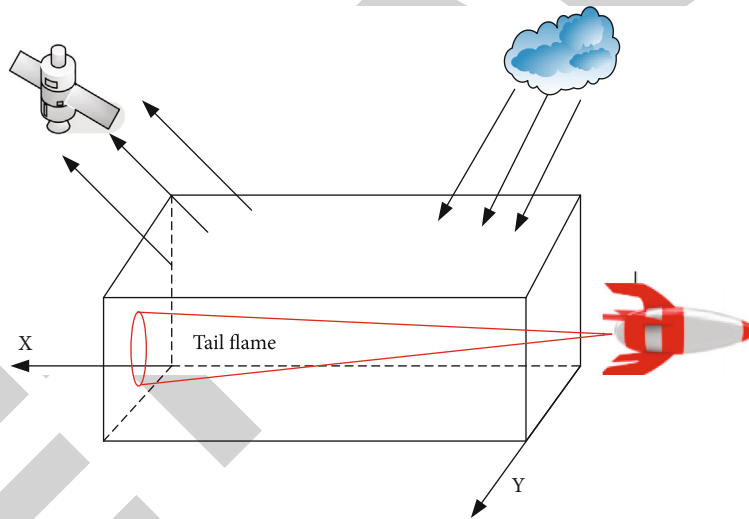


FIGURE 1: Geometry and physical model of engine exhaust flame.

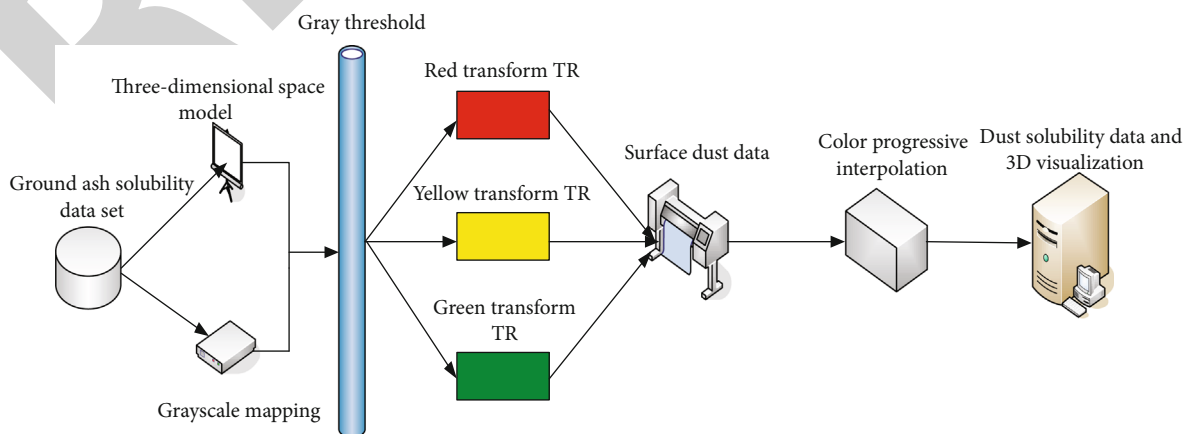


FIGURE 2: Visualization algorithm flow of engine tail flame.

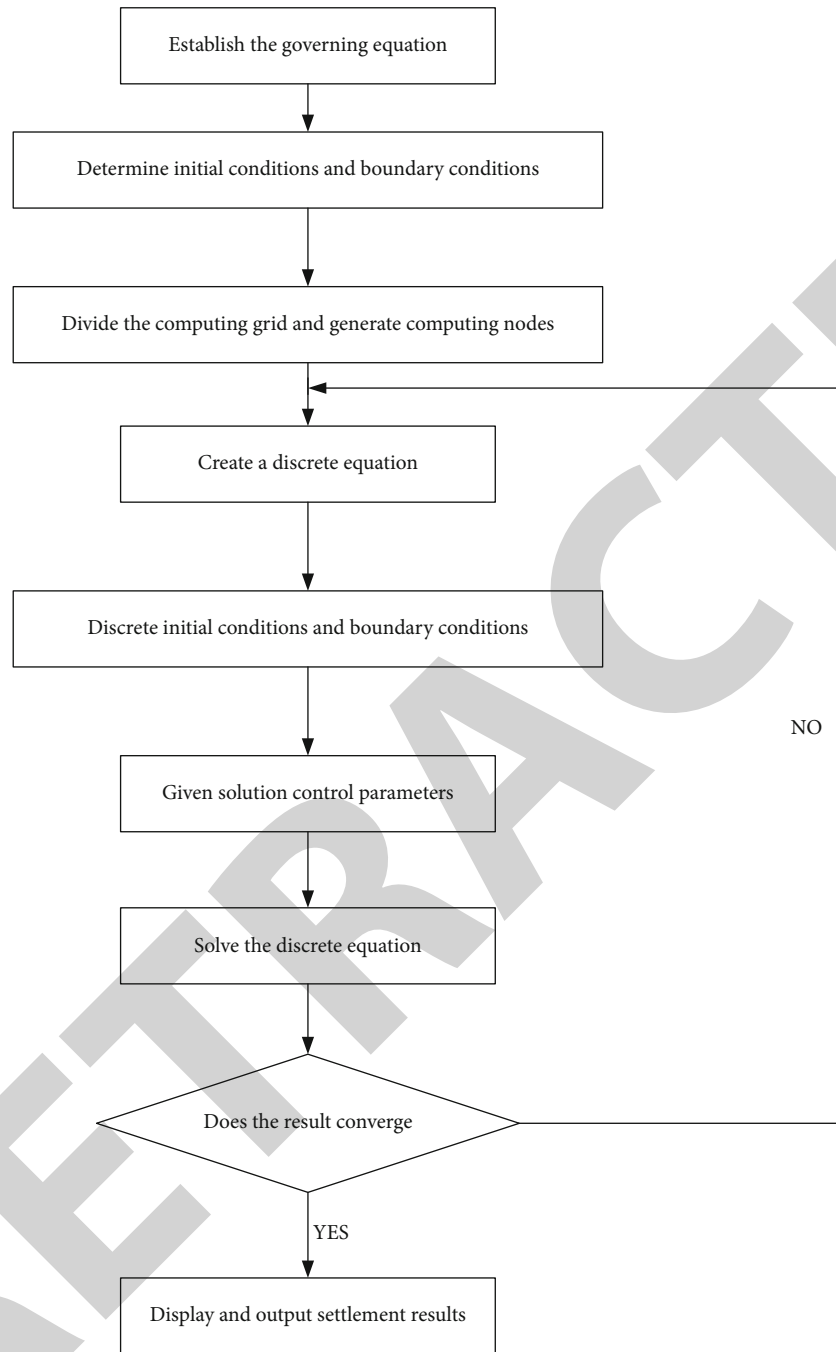


FIGURE 3: Solution flow chart.

The third-order polynomial calculation method is  $f_i(x)$  as follows:

$$f_i(x) = a_i + b_i(x - x_i) + c_i(x - x_i)^2, \quad (9)$$

where  $x$  is the spatial position of the pixel value of the point to be interpolated, the average value of the sum of  $x$ ,  $x_i$  and  $x_{i+1}$ , the calculation formula for the coefficient  $a_i$ ,  $b_i$ , and  $c_i$  calculation is

$$a_i = I(i, j), \quad (10)$$

$$b_i = I(i + 1, j) - I(i, j) - \frac{M_{i+1} - M}{6}, \quad (11)$$

$$c_i = \frac{M_i}{2}. \quad (12)$$

In the formula,  $I(i, j)$  is the intensity value  $(i, j)$  of the position pixel, which  $M_i$  is the second derivative  $f_i(x)$  of the equation.

**2.4. Kriging Interpolation.** Simple Kriging is a direct extension of the traditional linear regression theory, which believes that two different points in space are

TABLE 2: Immulation of oxidation reaction mechanism.

Component	Combustion chamber	Freedom
H <sub>2</sub> O	0.265	0
CO <sub>2</sub>	0.216	0
CO	0.107	0
H <sub>2</sub>	0.003	0
HCl	0.258	0
O <sub>2</sub>	0	0.221
OH	0	0
N <sub>2</sub>	0.105	0.756
H	0	0
O	0	0

interdependent. Its key is to estimate the unknown quantity at the position by estimating the linear combination of  $n$  known quantities  $Z(x_i)$  ( $i = 1, 2, \dots, n$ ) near the point. In this way,  $Z(x_0)$  involves the mean and covariance of  $n + 1$  variables, one of which is the unknown quantity and  $n$  known quantities nearby [18]. Its mean is

$$E[Z(x_i)] = m_i \quad i = 0, 1, \dots, n. \quad (13)$$

Its covariance is

$$\text{Cov}[Z(x_i), Z(x_j)] = E[Z(x_i)Z(x_j)] - m_i m_j. \quad (14)$$

At that time  $i = j$ , the covariance in the above formula was the variance.

$$Z^*(x_0) = \lambda_0 + \sum_{i=1}^n \lambda_i Z(x_i). \quad (15)$$

Among them,  $\lambda_i$  is the coefficient  $Z(x_i)$  of the variable, and the fixed value  $\lambda_0$  is called the drift parameter, which  $Z^*(x_0)$  is the best estimate under the condition of using  $n$  known samples at  $x_0$ .

Because  $Z^*(x_0)$  is an unbiased estimate  $Z(x_0)$ , that is,  $Z(x_0)$ :

$$\lambda_0 = m_0 - \sum_{i=1}^n \lambda_i m_i. \quad (16)$$

Since the mathematical expectation of the estimation error is zero, let the variance  $\alpha_0 = 1$ ,  $\alpha_i = -\lambda_i$  ( $i = 1, 2, \dots, n$ ) of the estimation error be

$$E\left\{[Z(x_0) - Z^*(x_0)]^2\right\} = \sum_{i=0}^n \sum_{j=0}^n \alpha_j C(x_i, x_j). \quad (17)$$

To minimize the estimated variance, then this set of values must make the following formula true:

$$\frac{1}{2} \frac{\partial}{\partial \lambda_i} E\left\{[Z(x_0) - Z^*(x_0)]^2\right\} = \frac{1}{2} \frac{\partial}{\partial \lambda_j}. \quad (18)$$

Because  $\alpha_0 = 1$ ,  $\alpha_i = -\lambda_i$  ( $i = 1, 2, \dots, n$ ), then, there is

$$\sum_{i=1}^n \lambda_i C(x_i, x_j) = C(x_0 - x_j). \quad (19)$$

If  $Z(x)$  only satisfies the eigen hypothesis, but does not satisfy the second-order stationary hypothesis, the ordinary Kriging equations and ordinary Kriging variance expressed by the relationship between the covariance function and the variogram are

$$\begin{cases} \sum_{i=1}^n \lambda_i \gamma(x_i, x_j) + \mu = \gamma(x_i + x_0), \\ \sum_{i=1}^n \lambda_i = 1. \end{cases} \quad (20)$$

Three conditions are required for an interpolation process to succeed: (1) the basic data must be continuously defined. (2) If the basic data sampling is given, the value of any point on the continuous function can be calculated based on this. (3) The sampling point in the recalculation the above value should be the same as the original value. The most important one is the third point. It is not difficult for us to think that if the third point is to be met, the basis function of the interpolation is required to be orthogonal. Only in this way can the weight of other sampling points be guaranteed when the sampling points are interpolated. The value can be zero.

Simple Kriging is rarely used directly in calculations, because it assumes that the average value of the life process depends on the conditions of life and is known, but in practice, it is generally used to average [19]. It can be used in other forms of Kriging, such as reference Kriging and non-standard Kriging. In these ways, the data has changed and the average value is known. Kriging is to extend the ordinary Kriging of one variable to two or more variables, and it must be a cohesive zone in which these variables cooperate with each other. This approach is useful if variables with low test costs and large samples have world correlation in variables with high test values and few variables, so that it is even possible to improve very good samples as a result of the data obtained with power sampling [20].

It is proposed a hybrid interpolation algorithm which combines the respective advantages of the bi-three-dimensional spline interpolation algorithm to the Kriging interpolation algorithm, with the basic flow of its realization as

- (1) Obtain data information of known dust
- (2) Calculate the variation function of the experiment
- (3) Select an appropriate theoretical model of the variogram to perform parameter fitting and determine the parameters of the variogram
- (4) Choose an interpolation point  $x_0$

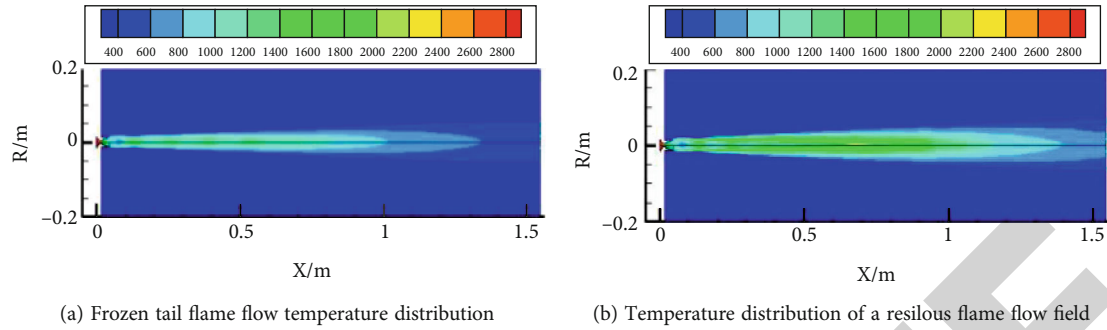


FIGURE 4: The temperature distribution cloud map of the tail flame under different conditions.

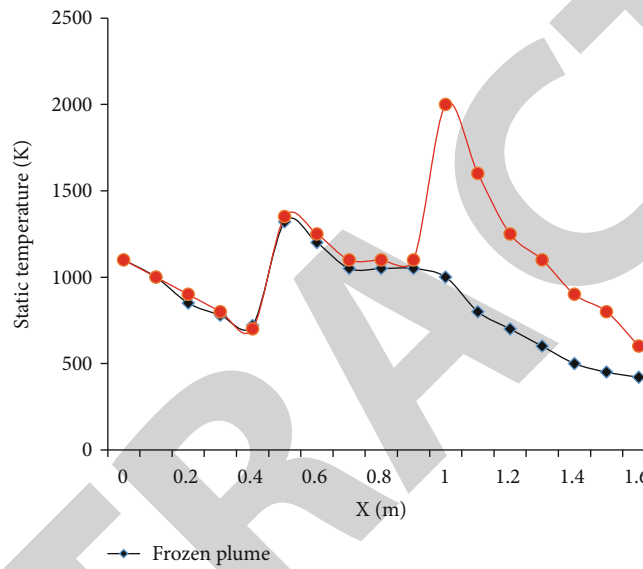


FIGURE 5: Temperature distribution of freezing flow and reburning flow on the axis of the plume.

- (5) Select the known sample points according to the search conditions  $x_i$
- (6) Calculate the corresponding weight coefficient according to the variation function  $\lambda_i$
- (7) Find the value of the interpolation point  $Z(x_0)$
- (8) Obtain the interpolation result

The main flow of the hybrid interpolation algorithm is shown in Figure 3.

### 3. Flame Visualization Experiment and Results

**3.1. Engine Tail Flame Parameters.** Considering ignition and reignition, the tail flame reaction flow range is used to accurately calculate the rocket engine flame freezing flow range. The entrance in the flow field calculation will be defined as a pressure entrance limitation state where the total pressure is 6 MPa, and the temperate is 3000 K. The output is defined as the far-field pressure limit state, the external free flow pressure is 101325 Pa, the Mach number is 1.5, and the tem-

perature is 300 K. The oxidation reaction mechanism is used for simulation calculation, and the reaction mechanism parameters used are shown in Table 2.

Numerical calculations are carried out for two different conditions of the freezing flow field and the reignition flow field of the rocket engine tail flame, and the temperature distribution cloud diagram of the tail flame under the two cases is obtained. The results are shown in Figure 4.

The temperature of the reignited and frozen tail flame flow field which is considered to reignite the rocket was obviously higher than that of an outer region near the tail flame flow field axis and in the middle and rear parts, with the high-temperature area of the reignited tail flame significantly larger to the frozen tail flame, which indicates that the reignition will raise the temperature of the tail flame flow field [21].

We performed statistics on the temperature distribution of the freezing flow and the reburning flow on the plume axis, and the results are shown in Figure 5.

It can be seen that the temperature of the reburning plume flow field is significantly higher than that of the freezing plume flow field by about 200~1000 K, and the

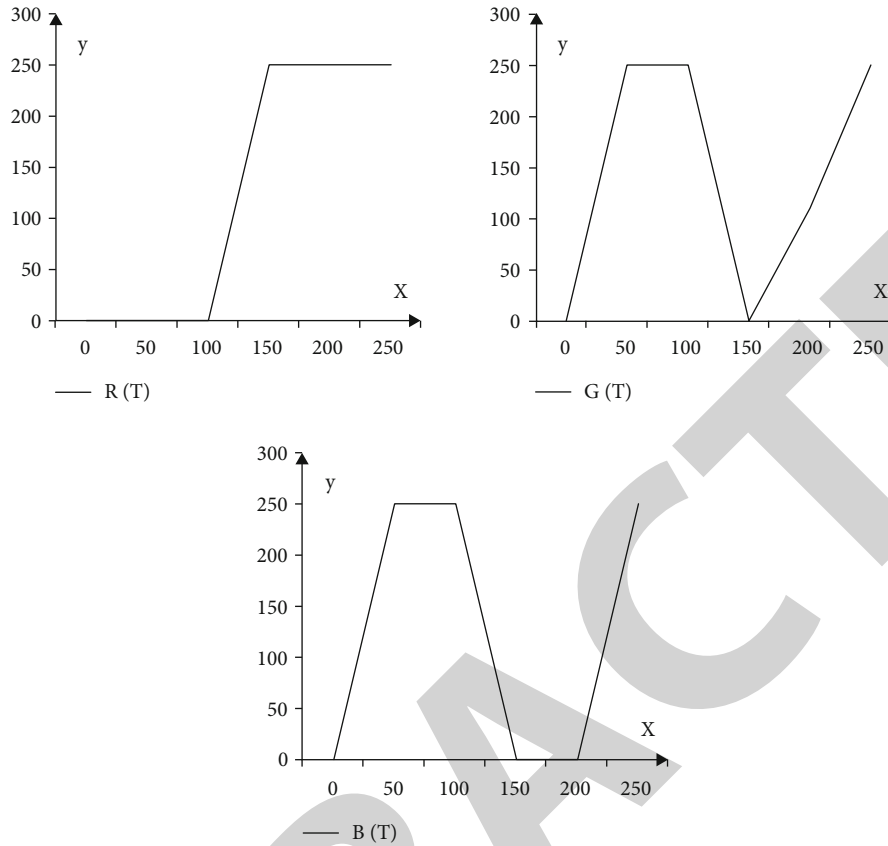


FIGURE 6: The weight coefficient function of the three primary colors.

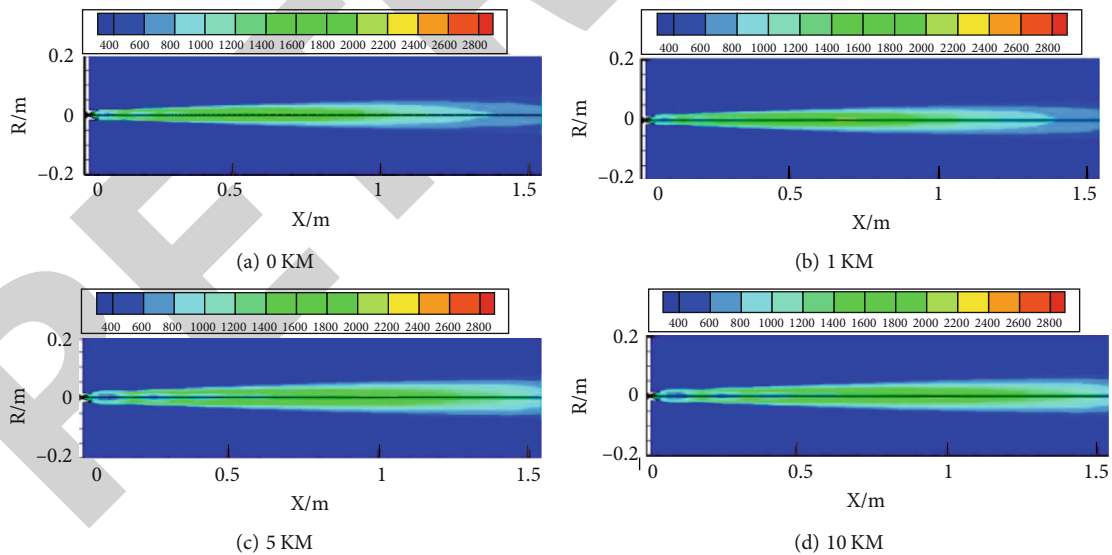


FIGURE 7: Engine exhaust flame temperature distribution at different flight altitudes.

reburning plume has a relatively obvious temperature peak at 0.7 m. In addition, a large amount on the heat of the chemical reaction is released, and the temperature of the tail flame rises, showing the significant effect of the rekindling on the temperature of the flame. Therefore, when calculating the rocket engine tail flame flow field, it is necessary to take into account the reignition of the gas jet and the oxygen in the free flow.

In the process of gray value map and color space system, the process of releasing the weight factor function of the first three colors is also used as the beginning of the construction work and process. The algorithm and the function image of the constructor used in this paper are shown in Figure 6.

In the definition constructor, the mapping with gray value less than 96 is dark red, the mapping with gray value

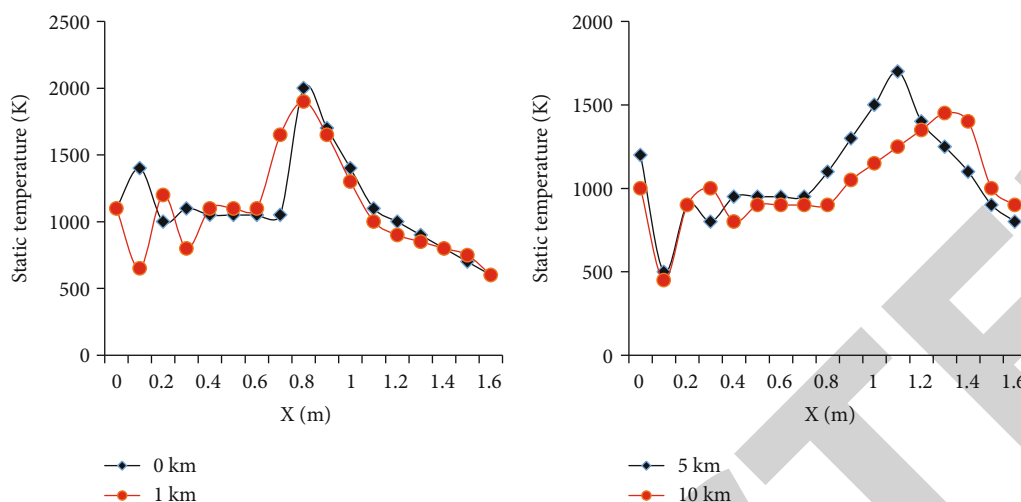


FIGURE 8: Temperature distribution of plume at different flight altitudes.

TABLE 3: Gas temperature in the combustion chamber under different working pressures.

Parameter	6 MPa	8 MPa	10 MPa	12 MPa	14 MPa
Temperature (K)	2624	2645	2657	2665	2671
H <sub>2</sub> O	0.1103	0.1041	0.1089	0.1027	0.1027
CO <sub>2</sub>	0.3419	0.3558	0.3707	0.3835	0.3963
CO	0.3312	0.3229	0.3126	0.3044	0.3062
H <sub>2</sub>	0.0127	0.0133	0.0149	0.0146	0.0151
O <sub>2</sub>	0	0	0	0	0
N <sub>2</sub>	0.1694	0.1694	0.1693	0.1694	0.1694
OH	0	0	0	0	0
H	0	0	0	0	0
O	0	0	0	0	0

greater than 128 is bright red, and the gray value between the two is the mapping process from dark red to bright red. In the same way, the gray value of the sum is also linearly mapped within a certain range.

**3.2. Visualization Research Calculation.** The temperature distribution in the exhaust flame flow field of the engine at different flight altitudes is shown in Figure 7.

Accompanied by the increase in flight altitude, since the outside ambient atmospheric pressure decreases that the expansion and diffusion of the flow field area intensifies, after the tail flame in the air reignition range also expands accordingly, and in the direction farther away from the nozzle outlet, reduce the temperature of the tail flame flow field, and reduce the degree of self-ignition [22, 23].

We compare the temperature distribution on the axis of the plume flow field under different flight altitudes, and the results are shown in Figure 8.

It can be seen that as the flying height increases, the maximum temperature near the inner axis of the first Mach wave system at the nozzle exit gradually decreases, and the position moves backward. This is because as the outside

atmospheric pressure decreases, the area of the space where the gas is sprayed from the nozzle with the Mach field flow structure expands and spreads to the space increases, resulting in an increase in the pressure and density of the gas near the nozzle outlet axis. The drop is more obvious, and the flow field temperature will drop. With the increase of flight altitude, the high-temperature area on the axis of the tail flame flow field caused by reignition moves to a direction farther from the nozzle outlet, the range expands, and the temperature of the tail flame increases significantly in the middle and downstream areas of the flow field [24].

The size of the calculation area of the tail flame flow field model is 1.5 m × 0.3 m, the inlet boundary condition is set as the pressure inlet, and the temperature is 3000 K. The outlet is set as the pressure far field boundary condition, the external free flow pressure is 101325 Pa, the temperature is 300 K, and the Mach number is 1.5 Ma. Obtain the temperature and mass fraction of each component in the combustion chamber, as shown in Table 3.

The comparison of the mass fraction of the tail flame flow field with different combustion chamber pressures is shown in Figure 9.

It can be seen that as the pressure of the combustion chamber increases, the degree of reignition of the solid rocket motor tail flame flow field increases, the temperature and spectral radiation intensity of the tail flame flow field increase, and the peak point gradually shifts back. The temperature and spectral radiation distribution was the area increases, and the temperature and radiation intensity at the Mach plate increase.

Calculations of the rocket engine in the tail flame temperature field have been investigated using numerical calculation methods, and the thermal considerations for four formulations of propellants are performed using the Gibbs minimum free energy method for the temperature of the gas and the gas component content in the combustion chamber, of which are shown in Table 4. The reignition phenomenon of the tail flame in the atmosphere is mainly composed of the oxidation reaction of carbon monoxide and

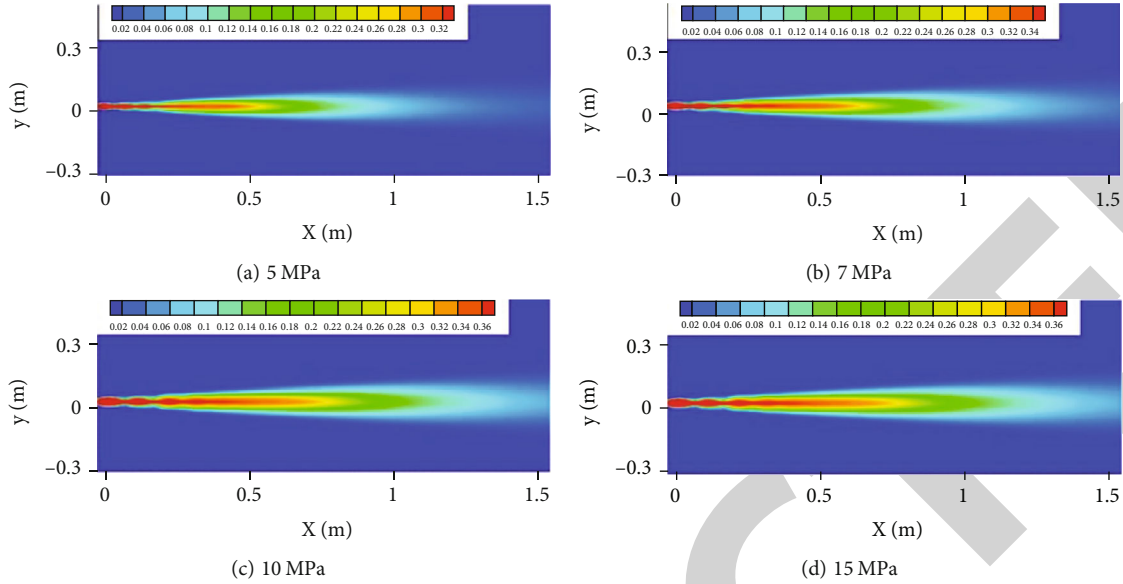


FIGURE 9: The tail flame flow field of different combustion chamber pressures.

TABLE 4: Formula of composite propellant with different ammonium perchlorate content.

Codename	Perchloric acid (g)	Aluminum powder (g)	HTPB (g)	Other (g)
AP-60	59	9	14	9
AP-65	64	9	14	9
AP-70	69	9	14	9

hydrogen. In this section, the hydrogen/carbon monoxide oxidation reaction mechanism is used for simulation calculation.

The comparison of the temperature distribution on the axis of the propellant tail flame with different aluminum powder content is shown in Figure 10:

With the increase of the aluminum powder content in the propellant, the temperature on the axis of the tail flame gradually increases within the range of 0-0.9m from the nozzle outlet, and the maximum temperature also increases. This is because after the aluminum powder content increases, the content of fuel-rich components CO and H<sub>2</sub> in the gas increases, thereby enhancing the degree of tail flame reignition and increasing the temperature peak. In addition, when the aluminum powder content in the propellant increases, the gas temperature in the combustion chamber will increase, and the gas temperature will increase. High-temperature particles move in the tail flame flow field. Thermal radiation and thermal convection heat the gas flow field.

## 4. Discuss

**4.1. Engine Exhaust Flame Temperature.** The compact rocket engines used in engineering practice have different flight speeds, flight altitudes, and working pressures. These conditions will have an impact on the flow field structure. Study-

ing the temperature field characteristics of the tail flame under these conditions will provide references for the design and development of engine engineering target recognition technology.

In addition, the flight speed of each rocket vehicle determines the relative motion between the flame and the surrounding atmosphere, which determines the temperature and pressure of the atmosphere surrounding the flame, which have important effects on the flashback of the flame and then the distribution of its thermostat.

This examination of the motor flow area was investigated, and the results obtained were used as a basis for the optimal design of the machine's combustion room and nozzle system. The rocket, which is launched and in flight, will furthermore produce multiple extra outdoor streams through this type of machine. Therefore, a numerical model for calculating the rocket field flow of a rocket device is proposed, and the parameter distribution of the training rocket field is the most important device and scientific value.

In this paper, the interpolation method is used to calculate the spectral radiation characteristics of the plume flow field and compare with the experiment. The calculation results are in good agreement with the experimental data, which shows the reliability of the calculation method. Calculate the flow field and spectral radiation characteristics of the frozen and regenerated tail flames and obtain the flow field parameters and spectral radiation distribution of the frozen and reburned tail flames, which reflect the spectral radiation characteristics of the refraction field. Calculations of the flow field and optical radiation characteristics have been carried out for the solid rocket tail flame at different flight speeds, elevation, and combustion chamber pressure to obtain the distribution of the tail flame flow field parameters and spectral intensity. With different conditions, this enables the analysis of the tail flame-radiation characteristics.

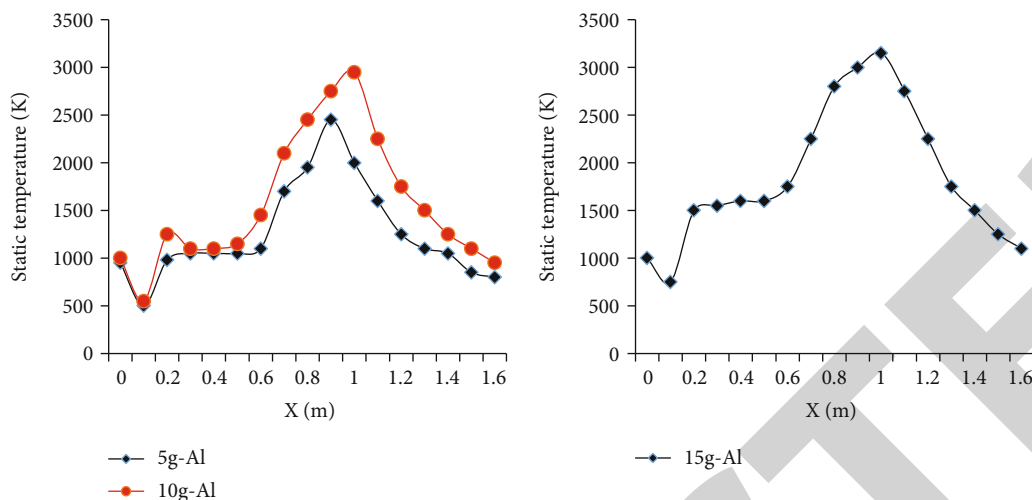


FIGURE 10: Comparison of the axis temperature of the propulsion tail flame.

**4.2. Interpolation.** The use of interpolation algorithms for image processing has received more and more attention from various countries and has been increasingly used in different fields. Polarization information is another important research object that is different from information such as frequency and amplitude. Information such as texture details can be received for this type of information through interpolation algorithms. Through experimental research, this paper establishes a polarized image generation and detection system, uses interpolation algorithm to process rocket engine tail flame images, and compares and analyzes the tail flame images processed by interpolation algorithm to achieve effective target identification.

The scientific research of bilinear, bicubic, and bicubic spline interpolation algorithms reveals the basis of mean square error, maximum signal-to-noise ratio and variance, and methods for analyzing composite images: information entropy, average gradient, and variance. The principle of these three dimensions is briefly explained, which lays the foundation for the subsequent processing, calculation, and analysis of the engine plume image.

Through the Kriging interpolation algorithm, the Kriging method is a linear, fair, and low conversion method. It is a statistical data based on system analysis in order to make full use of the characteristics of the database in the integration process. It can show the anisotropy of world data and make full use of the spatial compatibility between databases. The article introduces the types and characteristics of Kriging interpolation algorithms, mainly using Kriging interpolation technology to normalize and calculate data with related attributes. This part of the content is analyzed and summarized in detail, the normalized set is calculated with very clear data, and graphics and 3D images are presented. This will greatly help the decision-making and control aspects of the industry and related industries.

Based on bilinear, bicubic, and bicubic spline interpolation algorithm and Kriging interpolation algorithm, the algorithm is improved, and the feature selection method of the algorithm is improved. Because the recursive feature

removal process is combined with a specific learning model, and it still has a good effect when the data dimension is high, the recursive feature removal method is selected as the research direction of this article. This paper uses the effect of the hybrid algorithm as an evaluation criterion to evaluate each feature in the data set and implements a recursive feature removal method based on the hybrid algorithm. The feature selection method first uses all the features to establish a regression model, then ranks the contribution of each feature to the regression model, and gradually removes features that are not important to the regression analysis model, making the article achieve better results.

## 5. Conclusions

In the process of interpolating the surface dust concentration in the measurement area, this paper combines the advantages of the bicubic spline interpolation algorithm and the Kriging interpolation algorithm and proposes a new hybrid interpolation method that introduces the variation function and the azimuth search strategy. For the hybrid interpolation algorithm, this chapter gives a detailed implementation process and compares the results of the inverse distance hybrid interpolation algorithm and the inverse distance square interpolation algorithm, from the perspective of multiple test standards such as mean square error, deviation mean, and standard deviation. It proves that the hybrid interpolation algorithm is superior to the traditional algorithm. The method proposed in this paper can better realize the mapping of engine tail flame and color space system. This pseudoimage coding algorithm for visualizing dust density with smooth color transition is the color progressive interpolation method. This method performs layer segmentation on the three-dimensional space model of the engine exhaust flame based on the gray threshold and color space color clustering requirements and smooths the color transition between the layers. The advantages are (1) the data analysis is sufficient, which can meet different requirements. Models of rocket engine dynamic real-time

monitoring; (2) the proposed calculation method is simple and widely used, with high practicability, and is suitable for real-time processing applications; (3) the proposed method is highly malleable. Through real-time monitoring, the advantages of frame-by-frame analysis can be used for scientific research. Staff can continuously improve and optimize the design plan. This method can effectively predict the change law of engine tail flame characteristics. The overall results show that this method is scientific and effective. Compared with other traditional methods, the results are more robust and can provide more vivid data for future rocket engine research.

## Data Availability

No data were used to support this study.

## Conflicts of Interest

There is no potential conflict of interest in this study.

## References

- [1] S. Sreehari, S. V. Venkatakrishnan, B. Wohlberg et al., “Plug-and-play priors for bright field electron tomography and sparse interpolation,” *IEEE Transactions on Computational Imaging*, vol. 2, no. 4, pp. 408–423, 2016.
- [2] D. Kiku, Y. Monno, M. Tanaka, and M. Okutomi, “Beyond color difference: residual interpolation for color image demosaicking,” *IEEE Transactions on Image Processing A Publication of the IEEE Signal Processing Society*, vol. 25, no. 3, pp. 1288–1300, 2016.
- [3] W. Erb, C. Kaethner, M. Ahlberg, and T. M. Buzug, “Bivariate Lagrange interpolation at the node points of non-degenerate Lissajous curves,” *Numerische Mathematik*, vol. 133, no. 4, pp. 685–705, 2016.
- [4] R. McGranaghan, D. J. Knipp, T. Matsuo, and E. Cousins, “Optimal interpolation analysis of high-latitude ionospheric Hall and Pedersen conductivities: application to assimilative ionospheric electrodynamics reconstruction,” *Journal of Geophysical Research Space Physics*, vol. 121, no. 5, pp. 4898–4923, 2016.
- [5] P. Muhtarov and I. Kutiev, “Autocorrelation method for temporal interpolation and short-term prediction of ionospheric data,” *Radio Science*, vol. 34, no. 2, pp. 459–464, 1999.
- [6] C. Huang and Q. Chang, “Dissipativity of Runge-Kutta methods for dynamical systems with delays,” *IMA Journal of Numerical Analysis*, vol. 40, no. 11–12, pp. 1285–1296, 2004.
- [7] N. Totla and T. Wies, “Complete instantiation-based interpolation,” *Journal of Automated Reasoning*, vol. 57, no. 1, pp. 37–65, 2016.
- [8] G. T. S. Done, “Interpolation of mode shapes: a matrix scheme using two-way spline curves,” *Aeronautical Quarterly*, vol. 16, no. 4, pp. 333–349, 2016.
- [9] Z. Gao, X. Xu, Y. Su, and Q. Zhang, “Experimental analysis of image noise and interpolation bias in digital image correlation,” *Optics and Lasers in Engineering*, vol. 81, pp. 46–53, 2016.
- [10] G. S. Bhunia, P. K. Shit, and R. Maiti, “Comparison of GIS-based interpolation methods for spatial distribution of soil organic carbon (SOC),” *Agricultural Sciences*, vol. 17, no. 2, pp. 114–126, 2018.
- [11] T. P. Fries, S. Omerović, D. Schöllhammer, and J. Steidl, “Higher-order meshing of implicit geometries—part I: integration and interpolation in cut elements,” *Computer Methods in Applied Mechanics and Engineering*, vol. 313, pp. 759–784, 2017.
- [12] C. Kriegler and L. Weis, “Paley-Littlewood decomposition for sectorial operators and interpolation spaces,” *Mathematische Nachrichten*, vol. 289, no. 11–12, pp. 1488–1525, 2016.
- [13] S. Haghghatshoar and G. Caire, “Massive MIMO pilot decontamination and channel interpolation via wideband sparse channel estimation,” *IEEE Transactions on Wireless Communications*, vol. 16, no. 12, pp. 8316–8332, 2017.
- [14] J. Dolbeault, M. J. Esteban, M. Kowalczyk, and M. Loss, “Improved interpolation inequalities on the sphere,” *Discrete & Continuous Dynamical Systems - S*, vol. 7, no. 4, pp. 695–724, 2014.
- [15] Y. Huang, “Weighted tent spaces with Whitney averages: factorization, interpolation and duality,” *Mathematische Zeitschrift*, vol. 282, no. 3–4, pp. 913–933, 2016.
- [16] A. Bello, J. Reneses, A. Muñoz, and A. Delgado, “Probabilistic forecasting of hourly electricity prices in the medium-term using spatial interpolation techniques,” *International Journal of Forecasting*, vol. 32, no. 3, pp. 966–980, 2016.
- [17] S. Allavena, M. Piana, F. Benvenuto, and A. M. Massone, “An interpolation/extrapolation approach to X-ray imaging of solar flares,” *Inverse Problems & Imaging*, vol. 6, no. 2, pp. 147–162, 2012.
- [18] J. S. Cintra and C. L. Tucker III, “Orthotropic closure approximations for flow-induced fiber orientation,” *Journal of Rheology*, vol. 39, no. 6, pp. 1095–1122, 1995.
- [19] L. Demkowicz, P. Monk, L. Vardapetyan, and W. Rachowicz, “De Rham diagram for  $hp$  finite element spaces,” *Computers & Mathematics with Applications*, vol. 39, no. 7–8, pp. 29–38, 2000.
- [20] J. M. Melenk and C. Xenophontos, “Robust exponential convergence of  $hp$ -FEM in balanced norms for singularly perturbed reaction-diffusion equations,” *Calcolo*, vol. 53, no. 1, pp. 105–132, 2016.
- [21] H. Chen, Y. Shang, and K. Sun, “Multiple fault condition recognition of gearbox with sequential hypothesis test,” *Mechanical Systems and Signal Processing*, vol. 40, no. 2, pp. 469–482, 2013.
- [22] J. Zhao, J. Huang, Y. Xiang et al., “Effect of a protective coating on the surface integrity of a microchannel produced by micro-ultrasonic machining,” *Journal of Manufacturing Processes*, vol. 61, pp. 280–295, 2021.
- [23] J. Zhao, J. Huang, R. Wang, H. R. Peng, and S. Ji, “Investigation of the optimal parameters for the surface finish of k9 optical glass using a soft abrasive rotary flow polishing process,” *Journal of Manufacturing Processes*, vol. 49, pp. 26–34, 2020.
- [24] X. Xu, D. Cao, Y. Zhou, and J. Gao, “Application of neural network algorithm in fault diagnosis of mechanical intelligence,” *Mechanical Systems and Signal Processing*, vol. 141, 2020.